Solution Processable Fluorenyl Hexa-peri-hexabenzocoronenes in Organic Field-Effect Transistors and Solar Cells

14 AUTHORS, INCLUDING:

Wallace Wing Ho Wong
University of Melbourne
70 PUBLICATIONS **964** CITATIONS

SEE PROFILE

Thokchom Singh
The Commonwealth Scientific and Industri…
71 PUBLICATIONS **2,157** CITATIONS

SEE PROFILE

David John Jones
University of Melbourne
64 PUBLICATIONS **1,318** CITATIONS

SEE PROFILE

Andrew B Holmes
University of Melbourne
273 PUBLICATIONS **9,336** CITATIONS

SEE PROFILE

Solution Processable Fluorenyl Hexa-*peri*-hexabenzocoronenes in Organic Field-Effect Transistors and Solar Cells

By *Wallace W. H. Wong,* T. Birendra Singh, Doojin Vak, Wojciech Pisula, Chao Yan, Xinliang Feng, Evan L. Williams, Khai Leok Chan, Qinghui Mao, David J. Jones, Chang-Qi Ma, Klaus Müllen, Peter Bäuerle,* and *Andrew B. Holmes*

The organization of organic semiconductor molecules in the active layer of organic electronic devices has important consequences to overall device performance. This is due to the fact that molecular organization directly affects charge carrier mobility of the material. Organic field-effect transistor (OFET) performance is driven by high charge carrier mobility while bulk heterojunction (BHJ) solar cells require balanced hole and electron transport. By investigating the properties and device performance of three structural variations of the fluorenyl hexa-*peri*-hexabenzocoronene (FHBC) material, the importance of molecular organization to device performance was highlighted. It is clear from ^{1}H NMR and 2D wide-angle X-ray scattering (2D WAXS) experiments that the sterically demanding 9,9-dioctylfluorene groups are preventing π–π intermolecular contact in the hexakis-substituted FHBC 4. For bis-substituted FHBC compounds 5 and 6, π–π intermolecular contact was observed in solution and hexagonal columnar ordering was observed in solid state. Furthermore, in atomic force microscopy (AFM) experiments, nanoscale phase separation was observed in thin films of FHBC and [6,6]-phenyl-C61-butyric acid methyl ester (PC$_{61}$BM) blends. The differences in molecular and bulk structural features were found to correlate with OFET and BHJ solar cell performance. Poor OFET and BHJ solar cells devices were obtained for FHBC compound 4 while compounds 5 and 6 gave excellent devices. In particular, the field-effect mobility of FHBC 6, deposited by spin-casting, reached 2.8×10^{-3} cm^2 V^{-1} s and a power conversion efficiency of 1.5% was recorded for the BHJ solar cell containing FHBC 6 and PC$_{61}$BM.

1. Introduction

The performance of organic electronic devices depends heavily on the charge transport property of the organic semiconductor material employed. This is especially the case for organic field-effect transistors (OFETs) where charge carrier mobility correlates directly to device performance.[1] For organic solar cells (OSCs), the efficient transport of charges to the electrodes after exciton generation and charge separation is also a key factor in determining device efficiency.[2,3] Charge carrier mobility is a bulk material property. In organic materials, this is determined by the degree of aromatic conjugation and the intermolecular arrangement of the organic moieties. The orientation of molecules in the thin films can also affect the overall charge transport within a device. Planar polycyclic aromatic systems are increasingly employed in organic electronic devices mainly as a result of their excellent charge transport capability.[1] The most prominent example is the use of pentacenes[1,4,5] in OFETs while other fused acenes such as perylenediimides are gaining popularity as an n-type charge transport

[*] Dr. W. W. H. Wong, Dr. D. Vak, Dr. C. Yan, Dr. Q. Mao, Dr. D. J. Jones, Prof. A. B. Holmes
School of Chemistry, Bio21 Institute
University of Melbourne
30 Flemington Road, Parkville, Victoria 3010 (Australia)
Fax: (+613) 8344-2384; E-mail: wwhwong@unimelb.edu.au
Dr. T. B. Singh
CSIRO Molecular and Health Technologies
Ian Wark Laboratory
Clayton South, Victoria 3169 (Australia)

Dr. W. Pisula, Dr. X. Feng, Prof. K. Müllen
Max Planck Institute for Polymer Research
Ackermannweg 10, 55128, Mainz (Germany)
Dr. E. L. Williams, Dr. K. L. Chan
Institute of Materials Research and Engineering
3 Research Link, S(117602), Singapore (Singapore)
Dr. C.-Q. Ma, Prof. P. Bäuerle
Institut für Organische Chemie II und Neue Materialien
Universität Ulm
Albert-Einstein-Allee 11, 89081 Ulm (Germany)

© 2010 WILEY-VCH Verlag GmbH & Co. KGaA, Weinheim

WILEY InterScience®
DISCOVER SOMETHING GREAT

927

ADVANCED
FUNCTIONAL
MATERIALS
www.afm-journal.de

Materials Views
www.MaterialsViews.com

material.[6,7] There is also increasing interest in the use of zero bandgap graphenes in organic electronic devices.[8,9]

Discotic polycyclic aromatic molecules, such as hexa-*peri*-hexabenzocoronene (HBC), have shown promise as active components in OFETs as well as in OSCs. HBC is a planar aromatic molecule consisting of thirteen fused six-membered rings.[10,11] HBC and its derivatives have been shown to self-assemble into columnar structures giving rise to ordered morphology in films.[12,13] A mobility of 5×10^{-3} cm^2 V^{-1} s^{-1} was achieved in OFET devices using a dodecyl-substituted HBC molecule deposited by a zone casting technique that aids in the alignment of the molecules.[14] There have only been limited reports on the use of HBC's in organic solar cells.[15–19] Currently, most HBC derivatives rely on alkyl chains at the periphery for solubility, which limits the potential for further functionalization.[10,20–22] Even with the assembly of extended columnar structures, the peripheral alkyl chains of the HBC derivatives may adversely affect charge transport in the bulk material as they can create an insulating domain around the π–π stacked columnar core. Recently, we reported the synthesis and optoelectronic properties of highly soluble easily functionalized HBC building blocks carrying conjugated substituents.[23] The primary challenge in the synthesis of these systems is the incorporation of conjugated substituents as well as alkyl groups for solubility. The 9,9-dioctylfluorenyl hexa-*peri*-hexabenzocoronene (FHBC) moiety has emerged as a material with excellent solubility and the potential for further derivatization.[23] In this study, we report the optoelectronic and self-assembly properties of three FHBC molecules 4, 5, and 6

(Scheme 1). OFET and OSC devices with these FHBC materials were fabricated and their performance assessed. The relationships between molecular and bulk material structure, optoelectronic properties and device performance characteristics are discussed.

2. Synthesis, Characterization, and Optoelectronic Properties

The FHBC core molecules 4, 5, and 6 were readily obtained from previously reported FHBC compounds[23] 1, 2, and 3 (Scheme 1). The iodo substituents on the fluorene rings of compound 1, 2, and 3 were removed in high yield by transmetallation with *n*-butyl lithium (nBuLi) and protonation of the organolithium (see Experimental section for details). The UV–vis spectra of FHBCs 4, 5, and 6 in CH$_2$Cl$_2$ ($\sim$10^{-6} M) are shown in Figure 1a. FHBC 4 has a slightly red-shifted absorption maximum at 389 nm compared to FHBC 5 and 6 (Table 1). The onset of absorption of FHBC 4 is at the longest wavelength at 448 nm compared to that of FHBC 5 and 6 at 432 nm (Fig. 1a). The onset of absorption of these compounds was used to calculate the corresponding optical bandgaps. The onset of UV–vis absorption of the FHBC compounds in solid state are significantly red-shifted compared to the corresponding solution spectra (Fig. 1b, Table 1). This is indicative of molecular aggregation in solid state. There are significant differences between the thin film photoluminescence spectrum of the three FHBC compounds (Fig. 1c). While the first fluorescen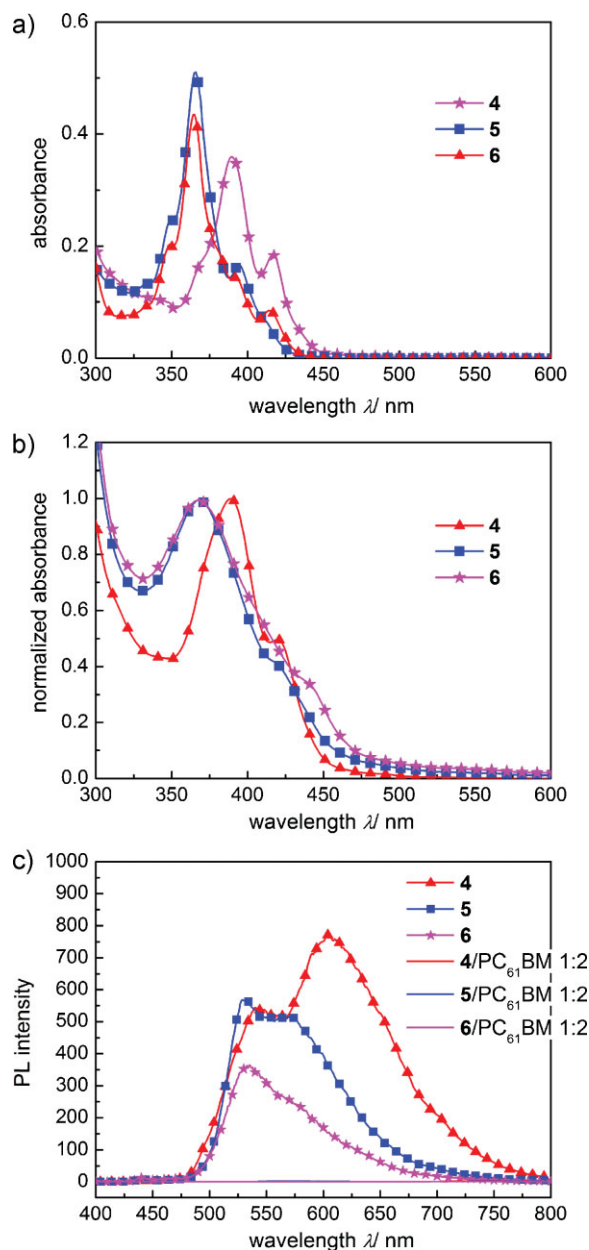ce peak reside at $\sim$530 nm for all three FHBC compounds, FHBC 6 has an additional emission at 600 nm. The fluorescence of all three compounds were completely quenched when blended with [6,6]-phenyl-C61-butyric acid methyl ester (PC$_{61}$BM) at a donor–acceptor ratio of 1:2 (w/w) (Fig. 1b). Electrochemical studies for these FHBC compounds were performed in dichloromethane solution. A summary of the electrochemical data can be found in Table 1 while cyclic voltammograms are provided in the Supporting Information. Energy level data of the three FHBC compounds indicate that these materials are suitable candidates for active layer blends with PC$_{61}$BM in bulk heterojunction solar cells (Fig. 2). It is interesting to note that the highest occupied molecular orbital (HOMO)– lowest unoccupied molecular orbital (LUMO) energy gap obtained in electrochemical experiments is slightly smaller compared to the optical energy gap for all three FHBC compounds (Table 1; Fig. 2).

3. Self-Assembling Properties and Solid State Morphology

Planar aromatic systems, such as hexa-*peri*-hexabenzocoronene (HBC), chiefly rely on π–π stacking as the force for self-assembly. In
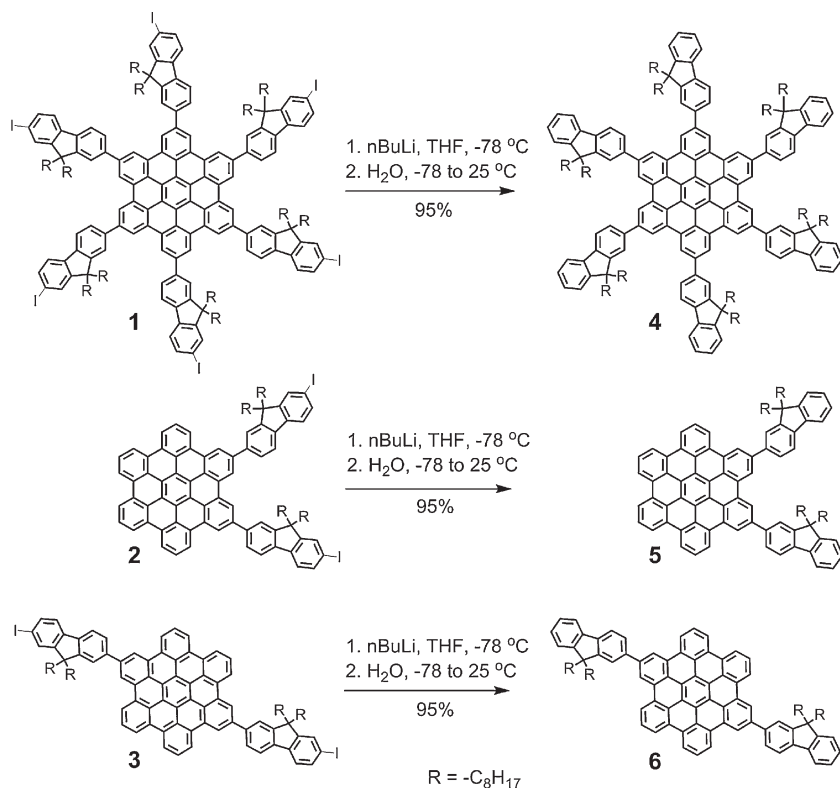
Scheme 1. Synthesis of 9,9-dioctylfluorenyl hexa-*peri*-hexabenzocoronene (FHBC) cores 4, 5 and 6. THF represents tetrahydrofuran.
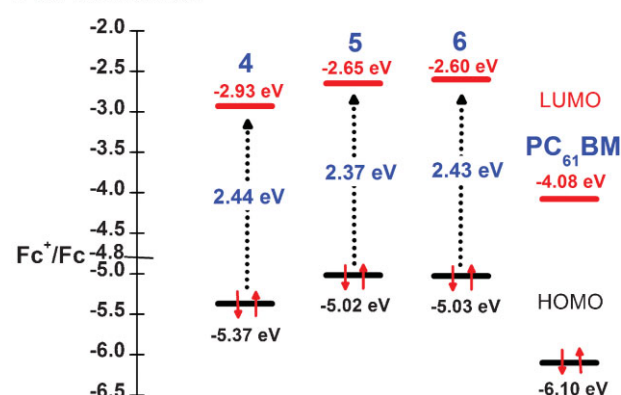
R = -C$_8$H$_{17}$

Materials
Views
www.MaterialsViews.com

ADVANCED
FUNCTIONAL
MATERIALS
www.afm-journal.de

FULL PAPER

Figure 1. UV–vis spectra of FHBC compounds **4**, **5**, and **6** a) in CH_2Cl_2 ($\sim 10^{-6}$ M) and b) as thin films. c) Thin film photoluminescence spectra of compounds **4**, **5**, and **6** and blends with $PC_{61}BM$ (1:2 w/w).

Figure 2. Energy level diagram of FHBC compounds **4**, **5** and **6** and $PC_{61}BM$. The data was derived from electrochemical experiments.

alkyl-substituted HBC systems, the long aliphatic chains provide solubility to the bulk material while they still allow π–π interactions between the aromatic cores of the molecules. The fluorenyl-substituted HBC derivatives in this study rely on the 9,9-dioctylfluorene units to impart solubility. The steric bulk of the 9,9-dioctylfluorenyl groups has the potential to hinder the π–π interactions of the aromatic cores. In the following ^{1}H NMR and 2D wide-angle X-ray scattering (2D WAXS) studies, the self-organization behavior of the three FHBC compounds are revealed.

^{1}H NMR spectra of the aromatic region for compounds **4**, **5**, and **6** are shown in Figure 3–5 respectively. Peak assignments were made primarily on the basis of the multiplicity of the peaks and by comparison with spectra of known material. The broadened resonances in ^{1}H NMR spectrum of FHBC **4** are probably a result of restricted rotations of the fluorenyl units around the HBC core. However, no changes in the NMR spectrum was recorded upon variation of the acquisition temperature of the NMR sample. The aromatic region of the ^{1}H NMR spectra of FHBC **5** and **6** changed significantly with concentration while the spectrum of FHBC **4** remained the same. For FHBC compounds **5** and **6**, it is clear that the protons assigned to the HBC core (H_x) shift upfield with increasing concentration (Fig. 4–5). The protons on the fluorene moiety which are closest to the core (F_1 and F_3) also shift upfield with increasing concentration. The upfield shift of these protons is due to a shielding effect caused by π–π stacking between FHBC molecules (Fig. 6).[13,24] An isodesmic model of indefinite stacking can be fitted to the changes in chemical shift with concentration.[25]

Table 1. Optical and redox data of the FHBC compounds.

Compounds	λ_{abs}^{max} [nm]		E_g^{opt} [eV] [a,b]	E_{ox}^{onset} [V] [c]	HOMO [eV] [d]	E_{red}^{onset} [V] [c]	LUMO [eV] [e]
	Solution [a]	Film					
4	389 (2.9)	391	2.76	0.57	−5.37 (−5.54)	−1.87	−2.93
5	367 (4.1)	370	2.87	0.22	−5.02 (−5.28)	−2.15	−2.65
6	364 (5.6)	368	2.87	0.23	−5.03 (−5.28)	−2.20	−2.60

[a] Measured in CH_2Cl_2 solution and extinction coefficient ($\times 10^5$ M^{-1} cm^{-1}) in parentheses. [b] Determined from the onset of absorption in solution. [c] In CH_2Cl_2, 1×10^{-3} M, Bu_4NPF_6 (0.1 M), 295 K, scan rate = 100 mV·s^{-1}, versus ferrocene/ferrocenium (Fc/Fc$^+$). [d] Determined from $E_{HOMO} = -(E_{ox}^{onset} + 4.80)$ [eV]; data in parentheses measured by photoelectron spectroscopy in air [47,48]. [e] determined from $E_{LUMO} = -(E_{red}^{onset} + 4.80)$ [eV].

ADVANCED
FUNCTIONAL
MATERIALS
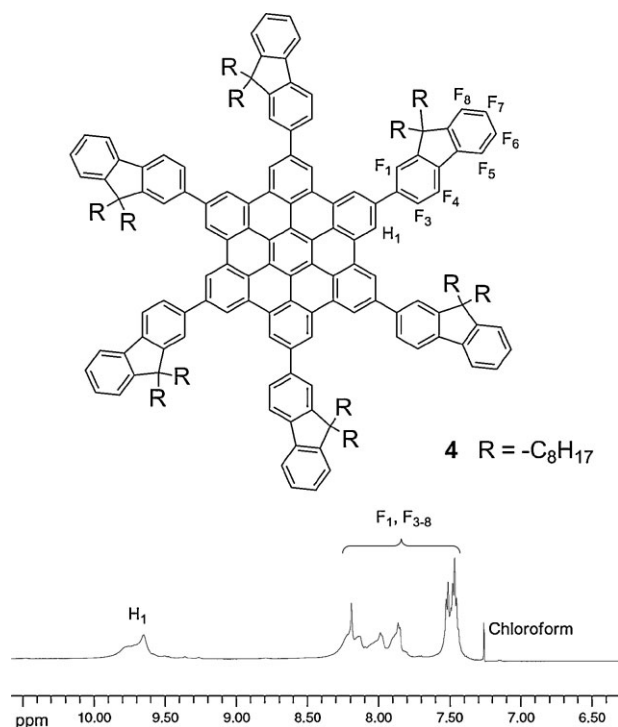www.afm-journal.de

Materials
Views
www.MaterialsViews.com

Figure 3. ^{1}H NMR spectrum of the aromatic region of FHBC **4**.
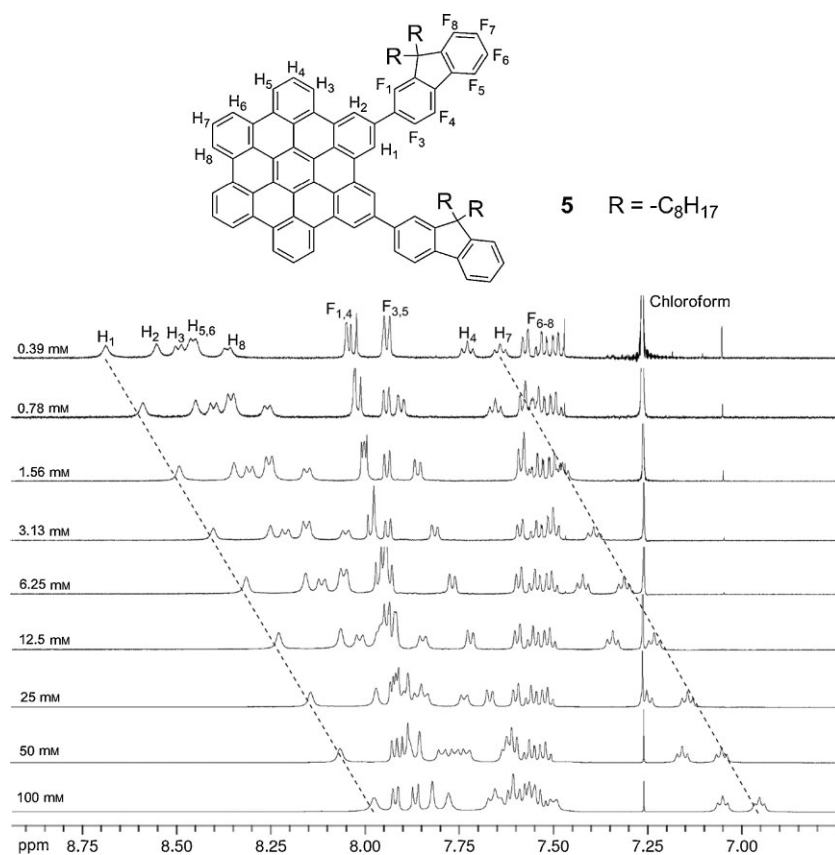
Figure 4. Concentration-dependent ^{1}H NMR spectra of compound **5** (CDCl$_3$ at 20 °C). Assignments of the spectra were primarily based on the multiplicity of the peaks and by comparison with spectra of known materials.
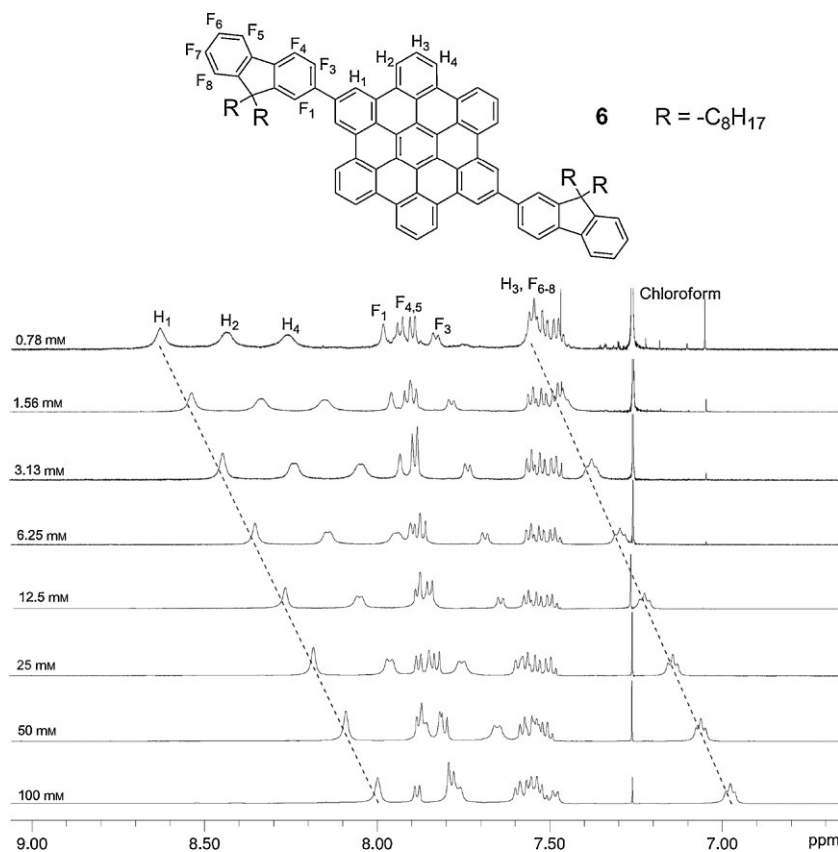
Association constants (K) were obtained by fitting the data to the equation for isodesmic model for stacking with equal association constants.[25] The chemical shift of the H$_1$ proton of the unassociated monomer (δ_{mono}) was arbitrarily set at 9 ppm while that of the aggregate (δ_{aggre}) was arbitrarily set at 8 ppm. Plots of concentration versus chemical shift for compounds **5** and **6** follow a similar trend, and the data fit well ($R^2 > 0.99$, see Supporting Information for details of the nonlinear curve fit) with the proposed indefinite stacking model (Fig. 6).

In order to gain insight into the solid state organization of the compounds **4**, **5**, and **6**, fiber WAXS experiments were performed (Fig. 7). The 2D pattern of FHBC **4** showed only one isotropic reflection which is related to a spacing of 2.3 nm (Fig. 7a). This distance is assigned to the formation of columnar structures due to most probably local phase separation between the alkyl side chains and the aromatic HBC cores. The absence of reflections correlated to the molecular packing indicates poor intermolecular associations and therefore no intracolumnar stacking. This is in agreement with the isotropic scattering intensity, which is characteristic of a macroscopically disordered sample. The weak order is related to the highly sterically demanding fluorenyl groups. It is well-known that bulky substituents can hinder the intracolumnar arrangement of disc-shaped building blocks. Previous studies on alkyl-substituted HBCs also revealed that bulky side chains reduce the π-stacking.[13,26,27] In contrast to FHBC **4**, co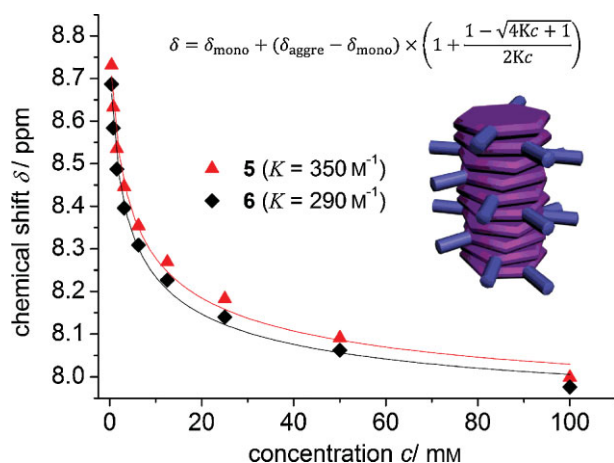mpounds **5** and **6** with only two fluorenyl substituents reveal a typical well-ordered columnar discotic liquid crystalline organization (Fig. 7b–c).[28,29] The equatorial reflections in both patterns suggest well-aligned columnar stacks along the fiber being arranged in a hexagonal manner to each other with $a_{hex} = 2.48$ nm for **5** and **6**. The equal unit cell parameter points out no influence of the substitution position of the two fluorenyl groups on the columnar and molecular packing due to a fast molecular rotation of the discs around the columnar axis in this liquid crystalline state. From the meridional reflections a π-stacking distance of 0.35 nm is derived for cofacially arranged discs of **5** and **6**. The liquid crystalline organization maintains over the whole investigated temperature range between −100 and +200 °C proving pronounced mesophase stability.

The surface morphology of thin films of FHBC compounds **4**, **5**, and **6**, spin-casted from chlorobenzene (25 mg/mL, 2000 rpm) on poly(3,4-ethylenedioxythiophene):poly(styrenesulfonate) (PEDOT:PSS)-coated silicon substrate, were examined using atomic force microscopy (AFM). No features were detected on the surface of the FHBC **4** film (Fig. 8). Thin films of FHBC **5** showed prominent crystallites while smaller crystalline features were detected for the FHBC **6** film. Thermal annealing at 150 °C for 30 min drove the formation of crystals in the samples containing FHBC **5** and **6** while the FHBC **4** film remained

www.MaterialsViews.com

ADVANCED
FUNCTIONAL
MATERIALS
www.afm-journal.de

FULL PAPER

6   R = -C$_8$H$_{17}$

Figure 5. Concentration-dependent ^{1}H NMR spectra of compound **6** (CDCl$_3$ at 20 °C). Assignments of the spectra were primarily based on the multiplicity of the peaks and by comparison with spectra of known materials.

$$\delta = \delta_{mono} + (\delta_{aggre} - \delta_{mono}) \times \left(1 + \frac{1 - \sqrt{4Kc + 1}}{2Kc} \right)$$

5 (K = 350 M^{-1})
6 (K = 290 M^{-1})

Figure 6. Variation in the ^{1}H NMR chemical shift of H$_1$ as a function of concentration for FHBC compounds **5** and **6**. The equation is derived from the isodesmic model for stacking with equal association constants [25].

smooth. These AFM results on thin films are in good agreement with the 2D WAXS experiments described above. Thin films of blends of FHBC compounds with PC$_{61}$BM (1:2) were also examined using AFM. Nanoscale phase separation was observed in all three blend films (Fig. 9). Smaller phase domain size for

FHBC **6**/PC$_{61}$BM film (∼50 nm) was observed compared to the other two films (>100 nm). Upon thermal annealing (150 °C, 15 s), there were changes in film morphology for the three samples (Fig. 9). The phase domains became larger for films containing FHBC **4** and **6** while there was a greater height contrast between the phase domains in the FHBC **5**/PC$_{61}$BM film. Extended thermal annealing time (150 °C, 30 min) promoted further phase separation in the samples containing FHBC **5** and **6** giving domain sizes greater than 1 μm (see Supporting Information for AFM images). These changes in film morphology have consequences to device performance and will be discussed in the following sections. It is worth noting that the thermal properties of the neat FHBC compounds were investigated using differential scanning calorimetry (DSC). No phase transitions were found for FHBC **4** and **6**. A weak transition was observed for FHBC **5** at 44 °C and can be attributed to the re-organization of the alkyl side chains (see Supporting Information for DSC data).

4. Field-Effect Transistors

The evidence of self-assembly of the discotic FHBC compounds into ordered structures in solid state provided extra impetus to study the relationship between molecular and bulk structure and charge transport properties. Charge mobility values for these materials can be obtained from their corresponding OFETs. In this study, bottom gate bottom-contact OFETs were fabricated by depositing the organic semiconductor from solution by spin-casting onto a lithographically patterned substrate (see Experimental for details). Good transistor behavior was observed for OFETs containing FHBC compounds **5** and **6** and their blends with PC$_{61}$BM (1:2 w/w) while OFETs with FHBC **4** showed rather poor device characteristics. A summary of charge mobility values for all OFET devices is presented in Table 2.

It is clear from the OFET data that FHBC **6** gave the best field-effect mobility both neat and as a blend with PC$_{61}$BM. With neat FHBC **6**, a mobility of 2.8×10^{-3} cm^2 V^{-1} s^{-1} with an on/off ratio of 2×10^5 was obtained. This compares favorably to a previously reported hexakisdodecyl-substituted HBC (mobility = 5×10^{-3} cm^2 V^{-1} s^{-1}, on/off ratio = 10^4).[14] In fact, the literature values were obtained from devices where the organic semiconductor layer was deposited using a zone-casting technique. This deposition technique drives the alignment of the molecules in a certain direction parallel to the substrate surface. In contrast, the FHBC compounds in this study are deposited by spin-casting. Deposition by spin-casting does not provide any spacial alignment of molecules and nano-aggregates of the FHBC molecules are likely to be randomly arranged in the thin films. In light of this, the field-effect mobility value of 2.8×10^{-3} cm^2 V^{-1} s^{-1} for compound **6** is impressive and there is potential for improvement.
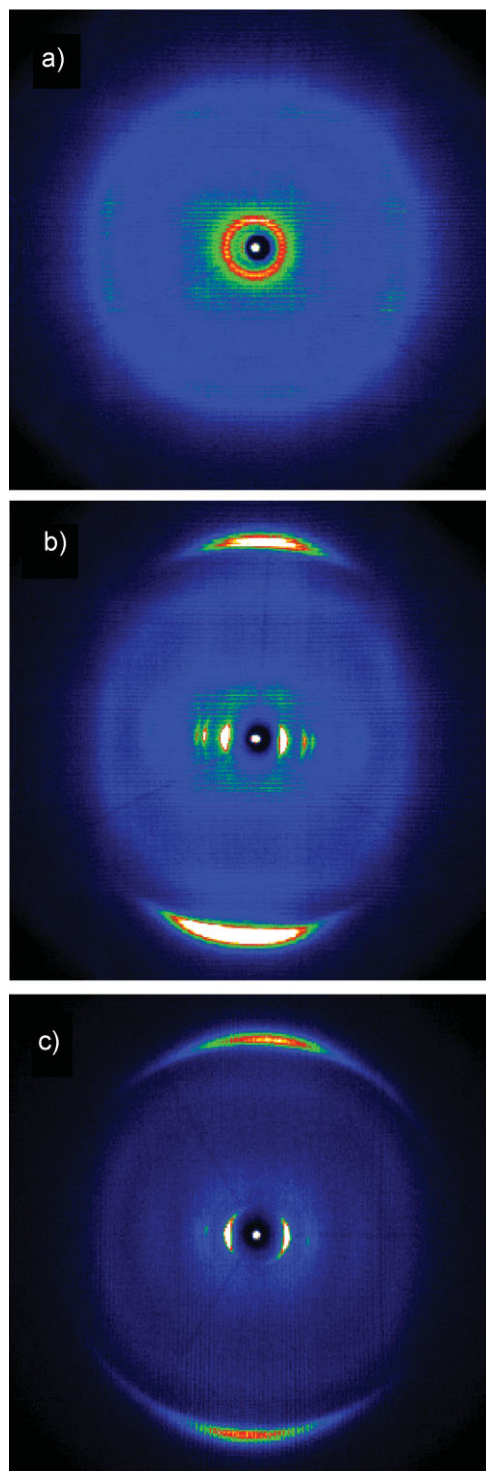
Figure 7. 2D WAXS patterns of a) **4**, b) **5**, and c) **6** at 30 °C.

Preliminary attempts to improve this field-effect mobility by thermal annealing did not change the mobility value significantly but the on/off ratio did improve from 2×10^5 to 6×10^6. It is interesting to note that the field-effect mobility for compound **6** is two orders of magnitude higher than compound **5** (Table 2). From
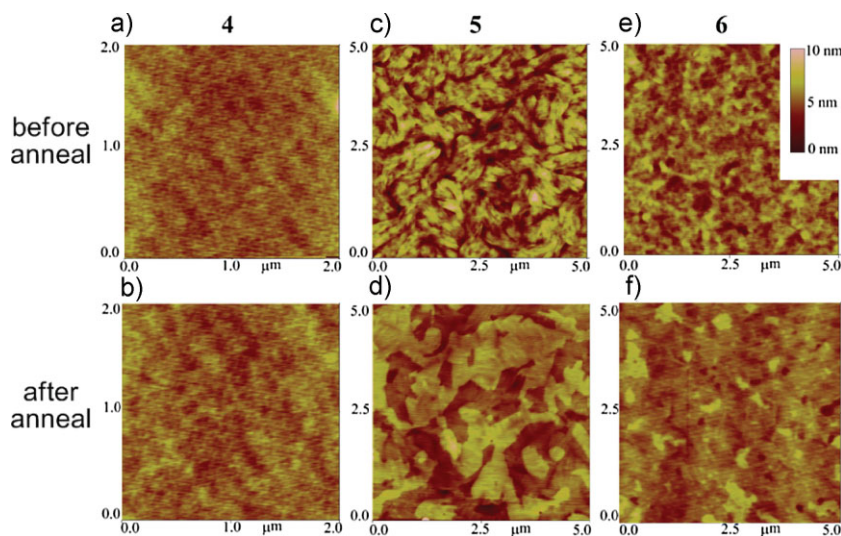
the ^{1}H NMR, 2D WAXS, and AFM studies presented above, there is no evidence to suggest the differences in self-organization and bulk ordering of the two materials would lead to such a large gap in OFET performance. In fact, it is surprising that the FHBC **5** film with the larger crystallites as observed with AFM (Fig. 8) did not perform better than FHBC **6** in the OFET devices. One possible explanation may be the fact that there are differences in the orientation of the columnar structures in thin films of compounds **5** and **6** which is a result of the inherent molecular structure difference between the two compounds. Apart from molecular orientation, interfacial contact between the semiconductor and the substrate and the electrodes can be influential on OFET performance. Further studies will be required to better understand this relationship between molecular structure, bulk structure and device performance. The poor performance of devices containing compound **4** can be attributed to the lack of ordered intermolecular arrangement as observed in the ^{1}H NMR, 2D WAXS, and AFM experiments. Investigations are now in progress to probe the molecular order in thin films of these FHBC compounds using X-ray diffraction.

The following section describes in detail the device characteristics of OFETs containing neat FHBC compound **6**. The transfer characteristics for OFET devices containing FHBC **4** and **5** can be found in the Supporting Information. The output and transfer characteristics of the OFET devices containing FHBC **6** are shown in Figure 10. Surface treatment of SiO$_2$ and metal contacts with octadecylsilanes (OTS) were performed to reduce the surface energy by hydrophobic nature of OTS. OTS is also thought to reduce the interfacial trap states.[30–33] Similarly, hexylmethasilazane (HMDS) is also used to passivate the Au/SiO$_2$ surfaces in order to obtain better adhesion of the organic semiconductor layer and saturate electron traps. Output characteristics of OTS-treated 20 μm channel length p-channel pristine FHBC **6** devices are shown in Figure 10a indicating well saturated drain currents, I_D as a function of drain voltage, V_D at $V_D \gg$ gate voltage, V_G. Transfer curves for three devices with different channel length (L) are shown in Figure 10b. All the devices show an on/off ratio of $\sim 10^5$. A plot of $\sqrt{I_D}$ versus V_G is presented in the bottom inset of Figure 10b. From the respective slopes, $\delta\sqrt{I_D}/\delta V_G$, L of 2.5–20 μm, channel width (W) of 10 mm, a capacitance per unit, C_i of 10 nF cm^{-2}, saturated field-effect mobility; μ, was calculated using Equation 1:

$$\mu = \frac{2L}{WC_i}\left(\frac{\delta\sqrt{I_D}}{\delta V_G}\right)^2 \tag{1}$$

Values of μ is in the range of 10^{-4}–10^{-3} cm^2 V^{-1} s^{-1} depending on the L were obtained as shown in the top inset of Figure 10b. Measurement on the HMDS-treated devices also yielded the same trend of L-dependent μ very similar to OTS-treated devices as shown in the top inset of Figure 10b. L-dependent μ has been reported by several groups recently.[34,35] In perfectly homogenous semiconductors, μ does not depend on L. In most common cases in OFET, μ increases with L owing to the presence of contact resistance. In an inhomogenous semiconductor, where charge transport is dominated by defects such as island and grain boundaries, μ decreases with L. In the present work, observation of decrease in μ with L predicts that the charge transport is not

Materials
Views
www.MaterialsViews.com

ADVANCED
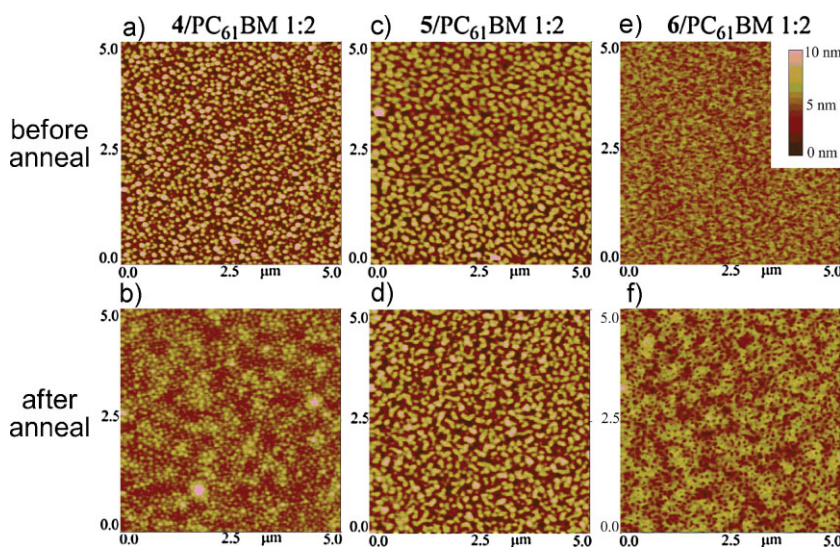FUNCTIONAL
MATERIALS
www.afm-journal.de

FULL PAPER

Figure 8. Morphology of pristine FHBC films on PEDOT:PSS-coated silicon substrate spin-casted from chlorobenzene with subsequent annealing at 150 °C for 30 min as imaged by tapping mode AFM: a,b) FHBC **4** before and after annealing; c,d) FHBC **5** before and after annealing; and e,f) FHBC **6** before and after annealing. The images (micrometer scale) display the surface topography (height in nm).

limited by the contact resistance, but instead is dominated by channel. This assumption is also supported by the observation of linear I_D–V_D curves at low V_D ($V_D \ll V_G$) in Figure 10a.

OFETs containing blends of FHBC compounds and $PC_{61}BM$ (1:2) were also fabricated by spin-casting. The OFET devices showed excellent ambipolar transport characteristics particularly for FHBC **6** (Fig. 11). From the AFM studies, there is clear phase separation between the donor and acceptor materials on the thin

film surface (Fig. 9). The ambipolar charge transport in these OFETs suggests that interpenetrating donor–acceptor domains exist in the thin films of these blends. Other techniques such as transmission electron microscopy (TEM) and electron tomography can be used in future studies to map the morphology in the thin films.[36] Transfer characteristics of ambipolar OFET containing FHBC **6** and $PC_{61}BM$ (1:2) on HMDS-treated SiO_2 are shown in Figure 11a. Electron and hole mobility in the range of 1.2×10^{-4} and $2.8 \times 10^{-4} V^{-1} s^{-1}$, respectively were obtained. Analogous to the transfer characteristics, ambipolar output characteristics are shown in Figure 11b. The I_D–V_D curves in the hole enhanced mode, at low V_G, channel current is predominantly electron only. At large V_G, hole only current flows in the channel at low V_D. At large V_D, electron current also contribute to the channel current. Similarly in the electron enhanced mode, channel current at low V_G is predominantly hole only current and followed by a rather large contribution of both electron and holes at large V_G and V_D. These results indicate that the present devices based on the blend of the two semiconductors are truly ambipolar in nature. In devices containing FHBC **4** and **5**, hole mobility was enhanced by the presence of $PC_{61}BM$, a phenomena which was previously observed but not yet understood fully (Table 2).[37] One other interesting observation from the FHBC **6**/$PC_{61}BM$ ambipolar OFET is that devices surface-modified with HMDS out-performed those modified with OTS. However, no significant difference in performance was observed for neat FHBC p-type semiconductors devices with either HMDS- or OTS-treated surfaces.

## 5. Bulk Heterojunction Solar Cells

Given all the optoelectronic and self-organization studies presented above, the FHBC derivatives appear ideal candidates to be employed as the electron donor material in BHJ solar cells. BHJ solar cells with the structure ITO|PEDOT:PSS|FHBC/$PC_{61}BM$ (1:2 w/w)|TiO_x/Al (where ITO is indium tin oxide) were fabricated and characterized. The ratio of donor and acceptor materials was optimized at 1:2 w/w while the active layer thickness was typically between 60 and 70 nm. TiO_x layers were introduced by following literature procedures.[38] In general, all devices showed good diode-like behavior in the dark and photovoltaic effects under simulated AM 1.5 G illumination. Table 3 summarizes the device performance of the various solar cells and the following characteristic parameters are given: short-circuit currents (J_{sc}), open-circuit voltages (V_{oc}), fill factors (FF), and power-conversion

Figure 9. Morphology of FHBC/$PC_{61}BM$ (1:2 w/w) blend films on PEDOT:PSS-coated silicon substrate spin-casted from chlorobenzene with subsequent annealing at 150 °C for 15 s as imaged by tapping mode AFM: a,b) FHBC **4**/$PC_{61}BM$ before and after annealing; c,d) FHBC **5**/$PC_{61}BM$ before and after annealing; and e,f) FHBC **6**/$PC_{61}BM$ before and after annealing. The images (5 μm × 5 μm) display the surface topography (height in nm) and share the same scale bars.

FULL PAPER

Table 2. Summary of parameters extracted from the OFETs fabricated using compounds **4**, **5** and **6** and their blends with PC$_{61}$BM (1:2 w/w) as semiconductor. The values shown here are the average of at least four different devices fabricated under identical conditions.

| Compounds	Surface modifier	Active layer	Mobility [cm^2 V^{-1} s^{-1}]	
			Hole	Electron
	HMDS	Neat	6.8×10^{-8} (1×10^3) [a]	–
4		Blend	–	–
	OTS	Neat	–	–
		Blend	1.3×10^{-7}	4.6×10^{-7}
	HMDS	Neat	3.3×10^{-6} (5×10^4) [a]	–
5		Blend	4.8×10^{-5}	2.2×10^{-7}
	OTS	Neat	3.2×10^{-5}	–
		Blend	2.1×10^{-5}	2.8×10^{-6}
	HMDS	Neat	2.8×10^{-3} (2×10^5) [a]	–
6		Blend	2.8×10^{-4}	1.2×10^{-4}
	OTS	Neat	2.3×10^{-3}	–
		Blend	4.5×10^{-6}	2.6×10^{-6}

[a] On/off ratio of the device.
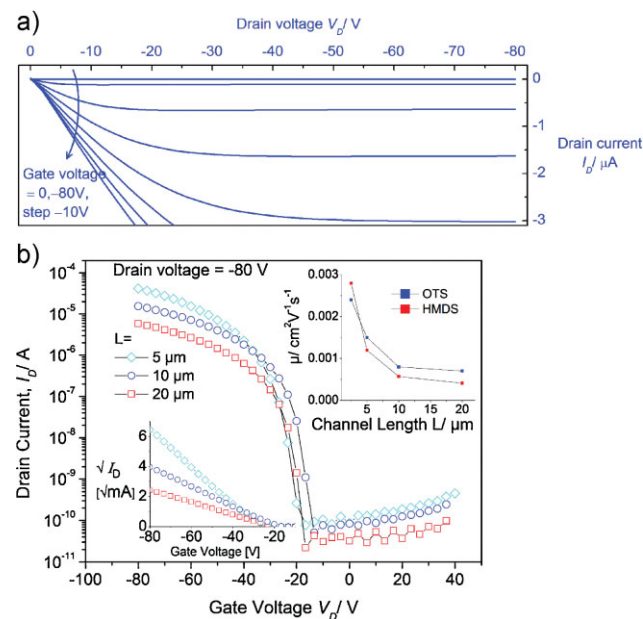
Figure 10. a) *p*-Channel output characteristics of OFET device containing compound **6** with OTS as the surface modifier. Channel length, $L = 20\,\mu m$ and W/L ratio = 500. b) Transfer characteristics in semilog plot of *p*-channel OFET device containing compound **6** with OTS as the surface modifier with different L values as indicated. Bottom inset shows transfer characteristics in square root plot as a function of gate voltage for different L values. Mobilities for various channel lengths (over ~4 devices per one channel) obtained from devices with compound **6** as the active material and either HMDS or OTS as surface modifiers are plotted in the top inset.

efficiencies (η). The data in Table 3 are average values over several devices. The current density to voltage curves and external quantum efficiency (EQE) spectra of selected devices are shown in Figure 12.

Overall, the device characteristics for the FHBC **4**/PC$_{61}$BM BHJ solar cell is poor compared to devices containing FHBC **5** and **6**.
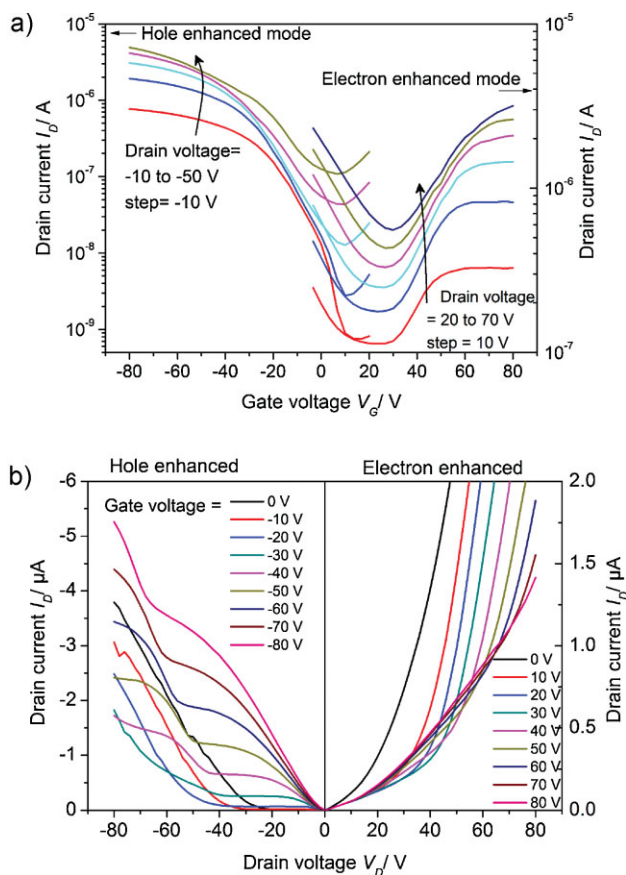
Figure 11. a) Ambipolar transfer characteristics in semilog scale of OFET device containing a blend of compound **6** and PC$_{61}$BM (1:2) with HMDS as the surface modifier. Channel length, $L = 20\,\mu m$. Note: left and right scale represents hole enhanced and electron enhanced mode respectively. b) Ambipolar output characteristics of OFET device containing a blend of compound **6** and PC$_{61}$BM (1:2) with HMDS as the surface modifier. Channel length, $L = 20\,\mu m$. Note: left and right scale represents hole enhanced and electron enhanced mode respectively. Mobilities obtained from the curves are summarized in Table 1.

Given that charge transport is a key factor in BHJ solar cell performance, the disordered bulk structure of compound **4** with respect to the highly ordered bulk structure of compounds **5** and **6**, as observed in the 2D WAXS experiments (Fig. 7), would account for most of the differences in device performance.

High V_{oc} of 0.9 V were observed for devices containing FHBC compounds **5** and **6** (Table 3). This is in agreement with the donor HOMO and acceptor LUMO energy gap of ~1 eV calculated from UV–vis spectroscopic and electrochemical experiments (Fig. 2). This is considerably better than typical V_{oc} of P3HT:PC$_{61}$BM BHJ solar cells (0.55–0.65 V).[39] The V_{oc} of devices containing FHBC **4** is considerably lower than the 1 V that one may expect from the donor HOMO and acceptor LUMO energy gap of ~1.3 eV (Fig. 2; Table 3). Despite the similar UV–vis absorption profiles of compounds **4**, **5**, and **6**, significant differences in the J_{sc} of the devices were recorded. Again, devices containing FHBC **4** gave a very low J_{sc} compared to devices containing **5** and **6**. With a similar number of photons absorbed, the difference in J_{sc} must be related to issues with charge separation, recombination and transport.

Materials
Views
www.MaterialsViews.com

ADVANCED
FUNCTIONAL
MATERIALS
www.afm-journal.de
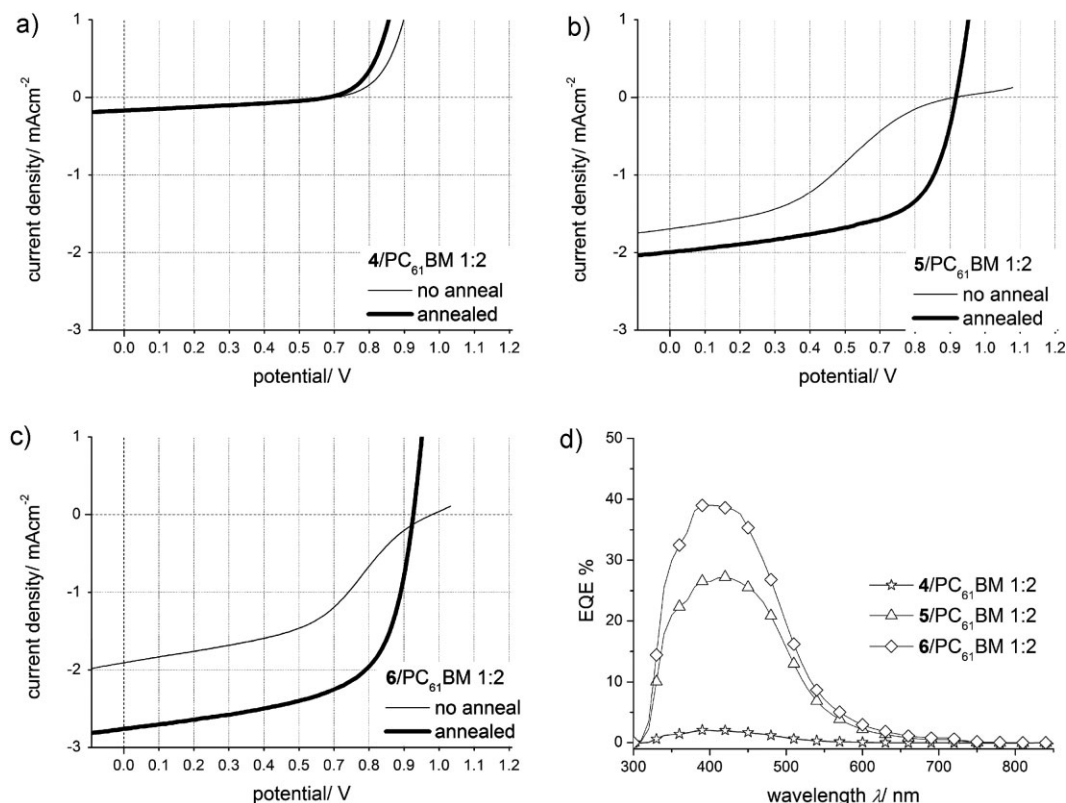
Figure 12. Current density–voltage curves of devices containing FHBC compound: a) **4**, b) **5**, c) **6**, and d) spectral response of annealed devices.

The spectral response of the devices is shown in Figure 12d. It is clear from this data that all devices harvest photons in the same wavelength range with maximum EQE at ∼400 nm. For the device with FHBC **6**, the maximum EQE is 39% while the maximum EQEs for FHBC **5** and **4** are 27% and 2%, respectively (Fig. 12d). By broadening the absorption range of these FHBC derivatives, in particular for FHBC **6**, there is potential to improve the J_{sc} and the overall efficiency of the BHJ solar cell device. The FF of a device is usually correlated to the balance between the transport of holes and electrons in the active layer. The FF of devices containing compounds **5** and **6** is superior to that of FHBC **4**. With thermal annealing (150 °C, 15 s), the FF for FHBC **5** and **6** devices improved to 0.6 on average reaching a maximum FF of 0.65 (Table 3). A FF value of 0.65 is comparable the best polymer/fullerene BHJ solar cells[3] and is significantly better than FF values (typically 0.4) for small molecule BHJ solar cell devices reported in the literature thus far.[19,40–43] Again, going back to the AFM images in Figure 9, some changes in nanoscale phase separation was observed after thermal annealing. In the case of the FHBC **6**/PC$_{61}$BM film, there is an increase in the domain sizes. However, this observation alone cannot explain the substantial improvement in the J_{sc} and FF of the BHJ devices. It is possible that thermal annealing increases molecular ordering (crystallinity) of the individual phase domains (both donor and acceptor) and improves the interfacial contact between the layers in the BHJ. These changes can lead to enhanced charge mobility and extraction and therefore higher J_{sc} and FF. The same reasoning can be applied to the improvements in the FHBC **5**/PC$_{61}$BM system after annealing. Although nanoscale phase

Table 3. Device performance of BHJ solar cells with active layers consisting of 1:2 FHBC/PC$_{61}$BM blends. Active layer thickness was 60–70 nm, and device area was 0.2 cm^2. The numbers shown are average values over several devices.

Donor	Annealing 150 °C, 15 s	V_{oc} [V]	J_{sc} [mA cm^{-2}]	FF	η [%] [a]
4	No	0.58	−0.18	0.31	0.03
4	Yes	0.61	−0.17	0.32	0.03
5	No	0.84	−1.69	0.37	0.53
5	Yes	0.87	−2.03	0.60	1.06
6	No	0.93	−1.87	0.45	0.78
6	Yes	0.90	−2.68	0.61	1.46

[a] $\eta = J_{sc} \times V_{oc} \times$ FF.

ADVANCED
FUNCTIONAL
MATERIALS
www.afm-journal.de

Materials
Views
www.MaterialsViews.com

separation was also observed for the FHBC **4**/PC$_{61}$BM blend films, the BHJ solar cells show very low performance. Thermal annealing did not improve this BHJ solar cell which can be related to the inherently low charge mobility of FHBC **4**.

Although there is still an ongoing debate on comparing OFET mobility with the charge mobility in diodes,[44] the results on bipolar OFETs correlate with the BHJ solar cell device performance in this study. There are significant difference in the device structure of the BHJ solar cell and the OFET devices. BHJ solar cell operation requires the transport of charges from the active layer to the electrodes in a direction perpendicular to the substrate while the charge movement in OFET is parallel to the substrate surface from the source electrode to the drain electrode. As discussed earlier, the nanoscale phase separation observed in AFM experiments suggests thin film morphology consisting of interpenetrating networks of the donor and acceptor materials. This can account for the correlation in the performance of the OFET and BHJ solar cell devices. For 1:2 blends of FHBC compound **6** and PC$_{61}$BM in OFETs, the hole carrier mobility is 2.8×10^{-4} cm^2 V^{-1} s^{-1} while the electron mobility is 1.2×10^{-4} cm^2 V^{-1} s^{-1}. This balanced hole and electron carrier mobility fits with the high FF of 0.65 observed in the same active material blend in the BHJ solar cell device. This correlation can be rationalized by the fact that balanced charge transport in donor–acceptor blends decreases the likelihood of electrical losses due to the recombination of slow charge carriers. Charge carrier recombination is one of the major factors influencing overall efficiency in BHJ solar cells. Interestingly, for devices containing 1:2 blends of FHBC **5** and PC$_{61}$BM, fill factor of over 0.6 was observed in the BHJ solar cells eventhough the charge carrier mobilities in the OFETs are lower and less balanced compared to the FHBC **6** devices. Studies are now in progress to examine the charge mobility in these BHJ solar cell devices using the photo-induced charge extraction by a linearly increasing voltage (photo-CELIV) technique.[45,46]

6. Conclusions

Three solution-processable fluorenyl hexa-*peri*-hexabenzocoronene (FHBC) derivatives were synthesized, characterized, and tested in OFET and BHJ solar cell devices. The bulky 9,9-dioctylfluorene unit affects intermolecular interactions in these materials and is essential in providing solubility and solution processability. The bis-substituted FHBC compounds **5** and **6** show strong self-assembly properties in solution and form hexagonal columnar ordering in solid state. The intermolecular association for hexakis-substituted FHBC **4** is much weaker in comparison. This is a result of steric hindrance of the fluorenyl units preventing π–π stacking of the planar hexa-*peri*-hexabenzocoronene disc. The degree of order of the bulk structure of these materials is reflected in their OFET and BHJ solar cell device performance. While FHBC **4** is a very poor material in both OFET and BHJ solar cell devices, the highly ordered structures of FHBC **5** and **6** gave excellent device performance characteristics. With FHBC **6**, a field-effect mobility of 2.8×10^{-3} cm^2 V^{-1} s^{-1} was achieved in spin-casted bottom-gate bottom-contact OFETs. BHJ solar cells containing FHBC **6** and PC$_{61}$BM reached a power conversion efficiency of 1.5% with thermal annealing.

Furthermore, a high fill factor of 0.65 was recorded. This fill factor is comparable to the best polymer/fullerene BHJ solar cells and is significantly better than other small molecular BHJ solar cell reported to-date. Work is now in progress to improve the field-effect mobility of these materials. New derivatives containing moieties with broad spectral absorption is also under preparation for application in BHJ solar cells.

7. Experimental

Compound Characterization: All reactions were performed using anhydrous solvent under an inert atmosphere unless stated otherwise. Silica gel (Merck 9385 Kieselgel 60) was used for flash chromatography. Thin layer chromatography was performed on Merck Kieselgel 60 silica gel on glass (0.25 mm thick). ^{1}H and ^{13}C NMR spectroscopy were carried out using either the Varian Inova-400 (400 MHz), the Varian Inova-500 (500 MHz) or the Bruker AMX 400 (400 MHz) instruments. Mass spectra were recorded with a MALDI-TOF MS Bruker Reflex 2 (DCTB as matrix). IR spectra were obtained on a Perkin Elmer Spectrum One FT-IR spectrometer while UV–vis spectra were recorded using a Cary 50 UV-vis spectrometer. Photoluminescence was measured with a Varian Cary Eclipse fluorimeter. Melting points were determined on a Büchi 510 melting point apparatus. Elemental analyses were obtained on a Perkin-Elmer EA 2400 (for C H) and commercially through CMAS, Victoria. Compounds **1**, **2**, and **3** have been reported in the literature [23]. All other compounds and reagents are commercially available.

Solid State Morphology Experiments: 2D WAXS experiments were performed using a Rigaku 18 kW rotating copper anode as source, and a double graphite monochromator to give CuKα radiation ($\lambda = 1.54$ Å). The X-ray beam was collimated using pinholes, and the scattered radiation was collected using a 2D Siemens detector. The samples were prepared by filament extrusion using a home-built mini-extruder. Therein, if necessary, the material is heated up to a phase at which it becomes plastically deformable and is extruded as 0.7 mm thin fiber by a constant-rate motion of the piston along the cylinder. Tapping-mode AFM (NanoScope II, Dimension, Digital Instrument Inc.) was carried out with commercially available tapping mode tips. The scanning area was between 10 μm × 10 μm and 1 μm × 1 μm. The AFM samples were prepared by spin-casting PEDOT:PSS (Baytron P AI 4083, 5000 rpm) on silicon substrate followed by the material of interest (25 mg/mL in chlorobenzene, 2000 rpm).

OFET Device Fabrication and Testing: A doped ($N \approx 3 \times 10^{17}$ cm^{-3}) Si wafer was used as a substrate and as gate electrode. Discrete bottom OFETs were fabricated on thermally grown smooth silicon dioxide (230 nm). Interdigitated source and drain electrodes were photolithographically patterned from a 50 nm sputtered gold layer. The *L* of the devices were varied between 2.5 and 20 μm where *W* is fixed at 10 mm. The SiO$_2$ layer was first cleaned with acetone and 2-propenol, and then treated with UV/ozone. It was immediately followed by a passivation layer of OTS or HMDS primer. OTS (1 mM in cyclohexane) was used and spin-coated at 4000 rpm. HMDS primer was spin-coated at 4000 rpm, followed by heating at 115 °C for 15 min prior to deposition of active organic semiconductor. Device fabrication was completed by spin-coating the organic semiconductor layers at 1500 rpm in air. The active layer consist of either pristine organic or blend with PC$_{61}$BM (1:2) in chlorobenzene (25 mg/mL). Without any further treatment, completed devices were transported inside a glove box fitted to probe the devices using a probe station. Electrical measurements were carried out using Keithley 2612 dual channel SMU. The reproducibility of the OFET preparation procedure is high with a confidence interval for the extracted mobility of ±15% of the values which have been presented. The carrier mobility values presented in this work are generally averaged from measurements done on at least four devices on the same substrate.

BHJ Solar Cell Device Fabrication and Testing: PEDOT:PSS (Baytron P AI 4083) was spin-coated (5000 rpm) on patterned ITO glasses which were

www.MaterialsViews.com

ADVANCED
FUNCTIONAL
MATERIALS
www.afm-journal.de

FULL PAPER

washed by detergent, deionized water, methanol, acetone, and 2-propanol in an ultrasonication bath and UV/ozone-treated. The films were baked at 150 °C for 5 min in air. Solution of FHBC compounds and PC$_{61}$BM (25 mg/mL) were prepared in chlorobenzene separately. The solution were stirred at 60 °C for 2 h and cooled down to room temperature before they were mixed together. Blend solutions (donor–acceptor 1:2) were made by mixing appropriate volumes of the solutions. The resulting solutions were stirred for 30 min and spin-coated (1500 rpm) on the PEDOT:PSS films. TiO$_x$ precursor solution (1:200 in methanol) was deposited on the active layer by spin-coating (2000 rpm) to form ∼10 nm of TiO$_x$ layer. The films were exposed to air for about 20 min at room temperature for hydrolysis or baked at 150 °C for 15 s (total air exposure time was about 10 min). The films were transferred to a metal evaporation chamber and aluminum (100 nm) were deposited through a shadow mask (active area was 0.20 cm^2) at approximately 1×10^{-6} torr. Film thickness was determined by Veeco Dektak 150+ Surface Profiler. The thickness of the photoactive layers was optimised for each of the donor–acceptor blends and was typically between 60 and 70 nm. The solar cells were illuminated at 100 mW cm^{-2} using 1 kW Oriel solar simulator with an AM 1.5G filter in air and *J–V* curves were measured using a Keithley 2400 source measurement unit. For accurate measurement, the light intensity was calibrated using a reference silicon solar cell (PVmeasurements Inc.) certified by the National Renewable Energy Laboratory. Spectral response was measured with a Keithley 2400 source meter, using monochromatic light from a Xe lamp in combination with monochromator (Oriel, Cornerstone 130). A calibrated Si cell was used as reference.

Synthesis of 2,5,8,11,14,17-hexakis(9,9-dioctyl-9H-fluoren-2-yl)hexabenzo[bc,ef,hi,kl,no,qr]coronene **4**: 2,5,8,11,14,17-hexakis(7-iodo-9,9-dioctyl-9H-fluoren-2-yl)hexabenzo[bc,ef,hi,kl,no,qr]coronene [23] **1** (0.2 g, 0.055 mmol) was dissolved in dry THF (50 mL) and cooled to −78 °C. *n*-Butyl lithium (0.15 mL, 2.5 M in hexanes) was added dropwise and allowed to stir at −78 °C for 15 min. Water (0.1 mL) was added and the reaction was allowed to warm from −78 °C to +25 °C over 30 min. Solvent was removed and the residual redissolved in CH$_2$Cl$_2$ (50 mL) and filtered through a plug of silica. The product was isolated as a yellowish brown powder (0.15 g, 95% yield) after precipitation from MeOH.

m.p. >250 °C. UV–vis: λ_{max} (thin film) = 391 nm. ^{1}H NMR (500 MHz, CDCl$_3$, 20 °C, δ): 0.79 (m, 36H, −CH$_3$), 1.00 (br, 24H, −CH$_2$−), 1.17 (br, 120H, −CH$_2$−), 2.26 (m, 24H, −CH$_2$−), 7.47 (m, 18H, ArH), 7.86–8.19 (m br, 24H, ArH), 9.66 (m br, 12H, HBC−H). ^{13}C NMR (125 MHz, CDCl$_3$, 20 °C, δ): 152.3, 151.4, 141.4, 141.0, 140.7, 131.3, 127.5, 127.2, 125.2, 123.3, 122.4, 121.5, 120.8 (2), 120.3, 55.8, 40.9, 32.1, 30.6, 29.6, 24.4, 22.9, 14.3. FT-IR (neat, cm^{-1}): 3058, 2952, 2922, 2851, 1606, 1581, 1455, 1368, 871, 829, 781, 738. Matrix-assisted laser desoprtion/ionization mass spectrometry, MS-MALDI (*m/z*): M$^+$ 2852.22. Elemental analysis (%): calcd. for C$_{216}$H$_{258}$, C 90.9, H 9.1; found C 91.0, H 9.0.

Synthesis of 2,5-bis(9,9-dioctyl-9H-fluoren-2-yl)hexabenzo[bc,ef,hi,kl,no,qr]coronene **5**: 2,5-bis(7-iodo-9,9-dioctyl-9H-fluoren-2-yl)hexabenzo[bc,ef,hi,kl,no,qr]coronene [23] **2** (1 g, 0.64 mmol) was dissolved in dry THF (50 mL) and cooled to −78 °C. *n*-Butyl lithium (1 mL, 2.5 M in hexanes) was added dropwise and allowed to stir at −78 °C for 15 min. Water (0.5 mL) was added and the reaction was allowed to warm from −78 to +25 °C over 30 min. Solvent was removed and the residual redissolved in CH$_2$Cl$_2$ (50 mL) and filtered through a plug of silica. The product was isolated as a yellow powder (0.8 g, 95% yield) after precipitation from MeOH.

m.p. >250 °C. UV–vis: λ_{max} (thin film) = 370 nm. ^{1}H NMR (500 MHz, 6.25 mM, CDCl$_3$, 20 °C, δ): 0.82 (t, *J* = 7 Hz, 12H, -CH$_3$), 1.01 (br, 4H, −CH$_2$−), 1.15 (br, 4H, −CH$_2$−), 1.24 (br, 40H, −CH$_2$−), 2.40 (m, 8H, −CH$_2$−), 7.31 (t, *J* = 7 Hz, 2H, HBC−H), 7.42 (t, *J* = 7 Hz, 2H, HBC−H), 7.55 (m, 6H, fluorine-H), 7.76 (d, *J* = 7 Hz, 2H, fluorene-H), 7.94 (m, 8H, fluorene-H and HBC−H), 8.06 (d, *J* = 8 Hz, 4H, HBC−H), 8.12 (d, *J* = 8 Hz, 2H, HBC−H), 8.15 (s, 2H, HBC−H), 8.31 (s, 2H, HBC−H). ^{13}C NMR (125 MHz, 75 mM, CDCl$_3$, 20 °C, δ): 151.4, 151.1, 141.2, 140.6, 140.3, 136.3, 128.3 (2), 128.2, 128.1, 126.5, 124.3, 122.8, 122.0, 121.4, 120.2, 120.0 (3), 119.8 (2), 118.4, 118.1, 118.0, 117.6, 55.4, 40.9, 31.9, 30.4, 29.6, 29.5, 24.4, 22.7, 14.2. FT-IR (neat, cm^{-1}): 3059, 2953, 2924, 2851, 1610, 1584, 1455, 1373, 1366, 1083, 1022, 866, 826, 781, 740, 684. MS-

MALDI (*m/z*): M$^+$ 1298.68. Elemental analysis (%): calcd. for C$_{100}$H$_{98}$, C 92.4, H 7.6; found C 92.4, H 7.6.

Synthesis of 2,11-bis(9,9-dioctyl-9H-fluoren-2-yl)hexabenzo[bc,ef,hi,kl,no,qr]coronene **6**: 2,11-bis(7-iodo-9,9-dioctyl-9H-fluoren-2-yl)hexabenzo[bc,ef,hi,kl,no,qr]coronene [23] **3** (1 g, 0.64 mmol) was dissolved in dry THF (50 mL) and cooled to −78 °C. *n*-Butyl lithium (1 mL, 2.5 M in hexanes) was added dropwise and allowed to stir at −78 °C for 15 min. Water (0.5 mL) was added and the reaction was allowed to warm from −78 to +25 °C over 30 min. Solvent was removed and the residual redissolved in CH$_2$Cl$_2$ (50 mL) and filtered through a plug of silica. The product was isolated as a yellow powder (0.8 g, 95% yield) after precipitation from MeOH.

m.p. >250 °C. UV–vis: λ_{max} (thin film) = 368 nm. ^{1}H NMR (500 MHz, 6.25 mM, CDCl$_3$, 20 °C, δ): 0.81 (t, *J* = 7 Hz, 12H, −CH$_3$), 0.99 (br, 4H, −CH$_2$−), 1.10 (br, 4H, −CH$_2$−), 1.24 (br, 40H, −CH$_2$−), 2.30 (m, 8H, −CH$_2$−), 7.30 (br t, 4H, HBC−H), 7.55 (m, 6H, fluorene-H), 7.68 (d, *J* = 7 Hz, 2H, fluorene-H), 7.88 (m, 6H, fluorene-H), 7.94 (br d, 4H, HBC−H), 8.14 (br d, 4H, HBC−H), 8.35 (br s, 4H, HBC−H). ^{13}C NMR (125 MHz, 75 mM, CDCl$_3$, 20 °C, δ): 151.5, 151.2, 141.1, 140.9, 140.2, 137.0, 128.6, 128.2 (2), 127.1, 127.0, 126.7, 124.5, 123.1, 122.9, 122.1, 121.7, 120.2, 120.0 (2), 119.9, 118.7, 118.1, 118.0, 55.4, 40.6, 31.9, 30.3, 29.5, 29.4, 24.3, 22.7, 14.2. FT-IR (neat, cm^{-1}): 3066, 2953, 2924, 2852, 1617, 1589, 1455, 1380, 1361, 816, 759, 740. MS-MALDI (*m/z*): M$^+$ 1298.59. Elemental analysis (%): calcd. for C$_{100}$H$_{98}$, C 92.4, H 7.6; found C 92.5, H 7.5.

[1] J. E. Anthony, *Angew. Chem. Int. Ed.* **2008**, *47*, 452.

[2] J. J. M. Halls, K. Pichler, R. H. Friend, S. C. Moratti, A. B. Holmes, *Appl. Phys. Lett.* **1996**, *68*, 3120.

[3] G. Dennler, M. C. Scharber, C. J. Brabec, *Adv. Mater.* **2009**, *21*, 1323.

[4] N. Bert, F. Matthias, S. Stefan, G. Martin, H. Martin, E. Christoph, L. Paolo, *Phys. Status Solidi A* **2008**, *205*, 526.

[5] D. J. Gundlach, J. E. Royer, S. K. Park, S. Subramanian, O. D. Jurchescu, B. H. Hamadani, A. J. Moad, R. J. Kline, L. C. Teague, O. Kirillov, C. A. Richter, J. G. Kushmerick, L. J. Richter, S. R. Parkin, T. N. Jackson, J. E. Anthony, *Nat. Mater.* **2008**, *7*, 216.

[6] J. H. Oh, H. W. Lee, S. Mannsfeld, R. M. Stoltenberg, E. Jung, Y. W. Jin, J. M. Kim, J.-B. Yoo, Z. Bao, *Proc. Natl. Acad. Sci.* **2009**, *106*, 6065.

[7] H. Yan, Z. H. Chen, Y. Zheng, C. Newman, J. R. Quinn, F. Dotz, M. Kastler, A. Facchetti, *Nature* **2009**, *457*, 679.

[8] K. S. Novoselov, A. K. Geim, S. V. Morozov, D. Jiang, Y. Zhang, S. V. Dubonos, I. V. Grigorieva, A. A. Firsov, *Science* **2004**, *306*, 666.

[9] S. Wang, P. J. Chia, L. L. Chua, L. H. Zhao, R. Q. Png, S. Sivaramakrishnan, M. Zhou, R. G. S. Goh, R. H. Friend, A. T. S. Wee, P. K. H. Ho, *Adv. Mater.* **2008**, *20*, 3440.

[10] J. Wu, W. Pisula, K. Müllen, *Chem. Rev.* **2007**, *107*, 718.

[11] P. Herwig, C. W. Kayser, K. Müllen, H. W. Spiess, *Adv. Mater.* **1996**, *8*, 510.

[12] S. Ito, M. Wehmeier, J. D. Brand, C. Kubel, R. Epsch, J. P. Rabe, K. Müllen, *Chem. Eur. J.* **2000**, *6*, 4327.

[13] M. Kastler, W. Pisula, D. Wasserfallen, T. Pakula, K. Müllen, *J. Am. Chem. Soc.* **2005**, *127*, 4286.

[14] W. Pisula, A. Menon, M. Stepputat, I. Lieberwirth, U. Kolb, A. Tracz, H. Sirringhaus, T. Pakula, K. Müllen, *Adv. Mater.* **2005**, *17*, 684.

[15] X. L. Feng, M. Y. Liu, W. Pisula, M. Takase, J. L. Li, K. Müllen, *Adv. Mater.* **2008**, *20*, 2684.

[16] J. P. Schmidtke, R. H. Friend, M. Kastler, K. Müllen, *J. Chem. Phys.* **2006**, *124*, 174704.

[17] J. Li, M. Kastler, W. Pisula, J. W. F. Robertson, D. Wasserfallen, A. C. Grimsdale, J. Wu, K. Müllen, *Adv. Funct. Mater.* **2007**, *17*, 2528.

[18] L. Schmidt-Mende, M. D. Watson, K. Müllen, R. H. Friend, *Mol. Cryst. Liq. Cryst.* **2003**, *396*, 73.

[19] L. Schmidt-Mende, A. Fechtenkotter, K. Müllen, E. Moons, R. H. Friend, J. D. MacKenzie, *Science* **2001**, *293*, 1119.

[20] J. Wu, A. C. Grimsdale, K. Müllen, *J. Mater. Chem.* **2005**, *15*, 41.

[21] Y. Yamamoto, T. Fukushima, Y. Suna, N. Ishii, A. Saeki, S. Seki, S. Tagawa, M. Taniguchi, T. Kawai, T. Aida, *Science* **2006**, *314*, 1761.

[22] J. P. Hill, W. Jin, A. Kosaka, T. Fukushima, H. Ichihara, T. Shimomura, K. Ito, T. Hashizume, N. Ishii, T. Aida, *Science* **2004**, *304*, 1481.

[23] W. W. H. Wong, D. J. Jones, C. Yan, S. E. Watkins, S. King, S. A. Haque, X. Wen, K. P. Ghiggino, A. B. Holmes, *Org. Lett.* **2009**, *11*, 975.

[24] J. Wu, A. Fechtenkotter, J. Gauss, M. D. Watson, M. Kastler, C. Fechtenkotter, M. Wagner, K. Müllen, *J. Am. Chem. Soc.* **2004**, *126*, 11311.

[25] R. B. Martin, *Chem. Rev.* **1996**, *96*, 3043.

[26] W. Pisula, M. Kastler, D. Wasserfallen, M. Mondeshki, J. Piris, I. Schnell, K. Müllen, *Chem. Mater.* **2006**, *18*, 3634.

[27] X. Feng, W. Pisula, T. Kudernac, D. Wu, L. Zhi, S. De Feyter, K. Müllen, *J. Am. Chem. Soc.* **2009**, *131*, 4439.

[28] S. Laschat, A. Baro, N. Steinke, F. Giesselmann, C. Hägele, G. Scalia, R. Judele, E. Kapatsina, S. Sauer, A. Schreivogel, M. Tosoni, *Angew. Chem. Int. Ed.* **2007**, *46*, 4832.

[29] S. Sergeyev, W. Pisula, Y. H. Geerts, *Chem. Soc. Rev.* **2007**, *36*, 1902.

[30] R. Ruis, A. Papadimitratos, A. C. Mayer, G. G. Malliaras, *Adv. Mater.* **2005**, *17*, 1795.

[31] B. S. Ong, Y. Wu, P. Liu, S. Gardner, *J. Am. Chem. Soc.* **2004**, *126*, 3378.

[32] S. Wo, B. Wang, H. Zhou, Y. Wang, J. Bessette, R. L. Headricka, A. C. Mayer, G. G. Malliaras, A. Kazimirov, *J. Appl. Phys.* **2006**, *100*, 093504.

[33] I. N. Hulea, S. Fratini, H. Xie, C. L. Mulder, N. N. Iossad, G. Rastelli, S. Ciuchi, A. F. Morpurgo, *Nat. Mater.* **2006**, *5*, 982.

[34] E. C. P. Smits, S. G. J. Mathijssen, P. A. van Hal, S. Setayesh, T. C. T. Geuns, K. A. H. A. Mutsaers, E. Cantatore, H. J. Wondergem, O. Werzer, R. Resel, M. Kemerink, S. Kirchmeyer, A. M. Muzafarov, S. A. Ponomarenko, B. de Boer, P. W. M. Blom, D. M. de Leeuw, *Nature* **2008**, *455*, 956.

[35] D. J. Gundlach, J. E. Royer, S. K. Park, S. Subramanian, O. D. Jurchescu, B. H. Hamadani, A. J. Moad, R. J. Kline, L. C. Teague, O. Kirillov, C. A. Richter, J. G. Kushmerick, L. J. Richter, S. R. Parkin, T. N. Jackson, J. E. Anthony, *Nat. Mater.* **2008**, *7*, 216.

[36] X. Yang, J. Loos, *Macromolecules* **2007**, *40*, 1353.

[37] R. Pacios, J. Nelson, D. D. C. Bradley, C. Brabec, *Appl. Phys. Lett.* **2003**, *83*, 4764.

[38] S. H. Park, A. Roy, S. Beaupré, S. Cho, N. E. Coates, J. S. Moon, D. Moses, M. Leclerc, K. Lee, A. J. Heeger, *Nat. Photon.* **2009**, *3*, 297.

[39] W. Ma, C. Yang, X. Gong, K. Lee, A. J. Heeger, *Adv. Funct. Mater.* **2005**, *15*, 1617.

[40] T. Rousseau, A. Cravino, T. Bura, G. Ulrich, R. Ziessel, J. Roncali, *Chem. Commun.* **2009**, 1673.

[41] C.-Q. Ma, M. Fonrodona, M. C. Schikora, M. M. Wienk, R. A. J. Janssen, P. Bäuerle, *Adv. Funct. Mater.* **2008**, *18*, 3323.

[42] A. B. Tamayo, X. D. Dang, B. Walker, J. Seo, T. Kent, T. Q. Nguyen, *Appl. Phys. Lett.* **2009**, *94*, 103301.

[43] B. Walker, A. B. Tamayo, X.-D. Dang, P. Zalar, J. H. Seo, A. Garcia, M. Tantiwiwat, T.-Q. Nguyen, *Adv. Funct. Mater.* **2009**, *19*, 3063.

[44] M. Morana, M. Wegscheider, A. Bonanni, N. Kopidakis, S. Shaheen, M. Scharber, Z. Zhu, D. Waller, R. Gaudiana, C. Brabec, *Adv. Funct. Mater.* **2008**, *18*, 1757.

[45] R. Österbacka, A. Pivrikas, G. Juska, K. Genevičius, K. Arlauskas, H. Stubb, *Curr. Appl. Phys.* **2004**, *4*, 534.

[46] A. J. Mozer, N. S. Sariciftci, L. Lutsen, D. Vanderzande, R. Österbacka, M. Westerling, G. Juska, *Appl. Phys. Lett.* **2005**, *86*, 112104.

[47] E. O. Kane, *Phys. Rev.* **1962**, *127*, 131.

[48] H. Kirihata, M. Uda, *Rev. Sci. Instrum.* **1981**, *52*, 68.